

ARTICLE

Rate-independent and ultra-stable low-temperature sodium storage in pseudocapacitive TiO₂ nanowires

Dongmei Lin,[‡]^a Kaikai Li,[‡]^a Qian Wang,^a Linlong Lyu,^a Baohua Li^{*b} and Limin Zhou^{*a}

Received 00th January 20xx,
Accepted 00th January 20xx

DOI: 10.1039/x0xx00000x

Sodium-ion batteries (SIBs) face with several challenges, including low capacity, short cycle life, and poor low-temperature performance. In this work, TiO₂-B/anatase dual-phase nanowires are synthesized and applied as SIB anode to address above challenges. For the first time, we find the excellent Na-storage performance of the nanowire anode like rate-independent capacities and ultra-stable cycling stability at low temperature. Operando Raman spectroscopy shows that the nanowires are completely amorphized after cycling at 303 K; however, the TiO₂-B phase of the dual-phase nanowires remains crystalline after cycling at 273 K. The different sodiation mechanism at different temperatures results in a lower capacity but a more stable structure during cycling at 273 K than at 303 K. Kinetic analysis shows that the nanowire anode possesses ultralow charge-transfer energy barrier and resistance with higher apparent Na diffusion coefficient at 273 K than at 303 K during desodiation, which significantly enhances the Na⁺ intercalation pseudocapacitive process at low temperature. The synergy between structural transition and diffusion kinetics leads to rate-independent and ultra-stable Na-storage performance at low temperature. This work provides new perspectives for the understanding and design of low-temperature SIBs with high rate capability and long cycle life.

Introduction

Energy storage is one of the most important research fields in the 21st century, with the goal of reducing society's dependence on fossil fuels.¹⁻³ Lithium-ion batteries (LIBs) have become the most rapidly developed and widely commercialized energy storage devices in the past 25 years and play an increasingly important role in electric vehicles (EVs).⁴⁻⁶ However, the growth of the global EV market has been much slower than initially predicted, which reflects the main challenges faced by the battery industry—extending the driving range (by increasing the energy density) and decreasing the price of EVs.^{4,7} These challenges have motivated battery researchers to achieve a significant breakthrough by substituting the current electrode materials with mass-produced high-capacity and low-cost electrode materials,^{7,8} which has been the focus of research in recent years. Regarding low-cost techniques, sodium-ion batteries (SIBs) are a viable alternative to LIBs because sodium (Na) resources are inexhaustible.⁸ Recent advances in SIBs suggest that some Na compounds have more promise than their lithium analogs.⁹⁻¹¹ However, SIBs are still limited by either poor cycling stabilities or low capacities.

In addition to exhibiting high energy density and extended cycle life, rechargeable batteries also need to provide stable output and rapid charge/discharge cycling at low temperatures, especially to power an EV or hybrid EV. However, in reality, rechargeable batteries, including both Li-ion batteries and Na-ion batteries, often experience significant capacity loss at low temperatures, which is a huge barrier, especially for EVs and aerospace applications. These limitations might be alleviated by the discovery of more suitable electrolytes and active materials.¹² Current efforts to improve the low-temperature performance of LIBs or SIBs have focused on increasing the ion transport kinetics in the electrolyte via formulation of the electrolyte by tuning its composition and additives.¹³⁻¹⁵ Few studies have investigated the low-temperature performance of electrode materials. Alberto Varzi *et al.* investigated the electrochemical activity of porous CuZn intermetallic alloys toward Li and showed that the CuZn alloys possess superior Li-storage capability at low temperature because of the high electronic conductivity provided by Cu and the porous electrode morphology.¹⁶ In addition, another study found that reducing the particle size of the LiFePO₄/C material can improve its low-temperature performance.¹⁷ Studies of SIB electrode materials at subzero are very rare. Ya You *et al.* studied Prussian blue as the SIB cathode material and found that it demonstrates outstanding low-temperature performance in terms of energy density, rate capability, and long cycle life at -25 °C.¹⁸ Guo *et al.* investigated Na₃V₂(PO₄)₂O₂F nano-tetraprisms as the SIB cathode material, which exhibits outstanding rate capability, ultra-long cycling stability, and superior low-temperature performance.¹⁹ Capacity retention of up to 76.4% at -25 °C and

^a Department of Mechanical Engineering, The Hong Kong Polytechnic University, Hong Kong, China. E-mail: mmlmzhou@polyu.edu.hk

^b Engineering Laboratory for the Next Generation Power and Energy Storage Batteries, Graduate School at Shenzhen, Tsinghua University, Shenzhen 518055, China. E-mail: libh@sz.tsinghua.edu.cn

† Electronic Supplementary Information (ESI) available. See DOI: 10.1039/x0xx00000x

‡ These authors contributed equally to this study.

0.2 C was achieved. However, to date, no study has investigated SIB anode materials, which is crucially to understand how temperature influences the Na-storage performance and to promote the future development and application of SIBs.

Some hard carbon and metallic antimony, tin, and their related compounds can exhibit high capacities, but these materials often face some important issues such as safety problems due to Na dendritic growth,²⁰ poor structural stability, and low rate capability due to the huge volume variation upon Na cycling.^{21, 22} Studies have shown that titanium dioxide (TiO₂) is an attractive, low-cost, and sustainable choice for use as an SIB electrode material, especially if high rate capabilities and negligible volume changes can be obtained.²³⁻²⁶ In this study, we develop TiO₂ nanowire SIB anode with two different phases in a single nanowire. The obtained TiO₂-B/anatase dual-phase nanowires exhibit excellent capacity, rapid charging capability, and long cycle life at low temperature, with better high-rate capacities at 273 K than those reported in the literature on TiO₂-based anodes at room temperature. The capacity performance of the dual-phase nanowire anode is nearly independent of the current density. Operando Raman spectroscopy, cyclic voltammetry (CV), temperature-dependent electrochemical impedance spectroscopy (EIS), and galvanostatic intermittent titration technique (GITT) analyses reveal that the excellent low-temperature Na-storage performance is induced by the stable structure during cycling, the ultra-low charge-transfer energy barrier and resistance, and the high apparent sodium diffusion coefficient during desodiation that improves the Na⁺ intercalation pseudo-capacitive process. We believe that this work provides a deeper understanding of the effect of low temperature on the structural transitions and Na-storage kinetics in SIB electrodes and can guide the future development of low-temperature SIBs.

Results and discussion

Morphology and structure of the dual-phase TiO₂ nanowires

The dual-phase TiO₂ nanowires were prepared using a facile and cost-effective hydrothermal method, as illustrated in Fig. 1a. The raw anatase TiO₂ nanoparticles with ~ 50 nm diameter (Fig. S1) were finally transformed into TiO₂ nanowires with two phases (anatase and TiO₂-B phases). The morphology and structure of the dual-phase TiO₂ nanowires were characterized by scanning transmission electron microscopy (STEM). Fig. 1b shows that the length of the dual-phase nanowires was several hundreds of nanometers and that the diameter was less than 10 nm. The high-resolution transmission electron microscopy (HRTEM) images in Fig. 1c and S2 show the coexistence of lattice fringes of the TiO₂-B phase [(001) plane d-spacing of ~ 0.65 nm] and the anatase phase [(101) plane d-spacing of ~ 0.35 nm, (103) plane d-spacing of ~ 0.24 nm] in a single nanowire. The coexistence of two phases in a single nanowire induced the formation of heterogenous interfaces. The red curves in Fig. 1c

show that several phase boundaries were present in the nanowire samples because the TiO₂-B phase was not continuously distributed in the nanowire. Nanowires consisting of pure anatase (A) phase and TiO₂-B (B) phase were also prepared by changing the temperature of heat treatment. As shown in Fig. S3, only lattice fringe of TiO₂-B phase or lattice fringe of anatase phase can be identified in the two samples, meaning that the nanowires are composed of pure TiO₂-B phase (Fig. S3a) or pure anatase phase (Fig. S3b). Heterogeneous interfaces generated from two phases have been reported to improve Li ion diffusion.²⁷⁻²⁹ They can also improve Na⁺ diffusion and consequently enhance the Na-storage capacity at high rates as reported recently.^{30, 31} This is also demonstrated by the following comparative study of the electrochemical performance using nanowires with different phases. The diffraction rings in the selected area electron diffraction (SAED) pattern shown in Figure 1d further confirm the coexistence of the two phases (A: anatase phase; B: TiO₂-B phase).

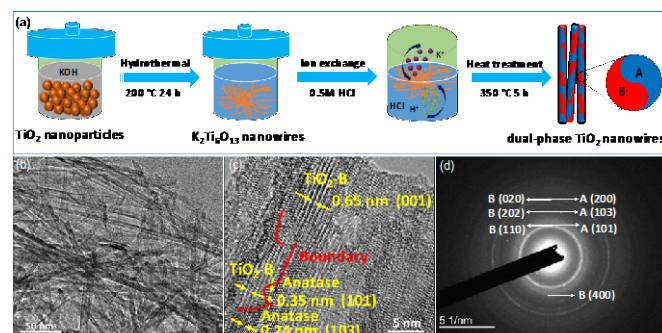


Fig. 1 (a) Schematic illustration of the fabrication process of the dual-phase TiO₂ nanowires. (b) STEM and (c) HRTEM images of the dual-phase TiO₂ nanowires. The yellow lines in (c) indicate the lattices of TiO₂-B and anatase phases, and the red line marks the interface between two phases. (d) SAED pattern with the anatase phase being designated as A and TiO₂-B phase as B.

Fig. 2a shows the X-ray powder diffraction (XRD) pattern of the obtained nanowires. The black and purple vertical lines mark the theoretical peak positions of the pure anatase phase (JCPDS 21-1272) and the pure TiO₂-B phase (JCPDS 74-1940). Indeed, the obtained nanowires comprise both the TiO₂-B and anatase phases. Fitting of the XRD pattern revealed the phase composition of the nanowires as 51 wt% TiO₂-B phase and 49 wt% anatase phase. The Raman spectrum in Fig. 2b also demonstrates the dual-phase characteristic of the obtained nanowires as the spectrum possesses Raman bands of both the TiO₂-B and anatase phases.³² Fig. S4 shows the X-ray photoelectron spectroscopy (XPS) spectrum of the dual-phase TiO₂ nanowires. The high-resolution XPS Ti 2p spectrum (Fig. 2c) and O 1s spectrum (Fig. 2d) show that the existence of Ti³⁺ in the dual-phase nanowires, indicating the presence of oxygen vacancies. These oxygen vacancies may have originated from

the two-phase interface or the surface of the nanowire and will provide additional active sites for Na-storage. Moreover, the Brunauer–Emmett–Teller (BET) results (Fig. S5) demonstrate that the dual-phase TiO₂ nanowires had a high surface area (171.01 m² g⁻¹). The large specific surface area results in larger contact area between the electrode and the electrolyte, which may be beneficial for rapid Na insertion/extraction.

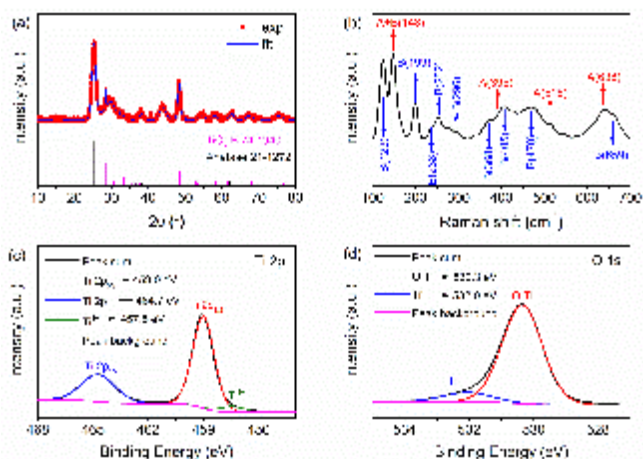


Fig. 2 (a) XRD pattern, (b) Raman spectrum, (c) XPS Ti 2p spectrum, and (d) XPS O 1s spectrum of the dual-phase TiO₂ nanowires.

Electrochemical performance

The dual-phase nature, heterogenous interface, small size, oxygen vacancies and high surface area are expected to endow the material with high capacity and high rate capability.^{27,33,34} Fig. 3 shows the electrochemical performance of the dual-phase TiO₂ nanowires for SIBs. Fig. S6 shows the first three charge–discharge voltage profiles at a rate of 0.25 C (1 C = 335 mA g⁻¹) between 0.01 V and 3 V at 303 K and 273 K. The charge–discharge curves show a continuous slope without plateaus at both temperatures, implying that the sodiation of the dual-phase TiO₂ nanowires was probably a single-phase transition process.³⁵ The first discharge and charge capacities were measured to be 438.5 and 305.3 mAh g⁻¹ at 303 K, respectively, resulting in an initial coulombic efficiency (CE) of 70%, which is much higher than that of other TiO₂-based electrodes reported in the literature (Table S1). When the temperature was decreased to 273 K, the first discharge and charge capacities were measured to be 340.9 and 173.6 mAh g⁻¹, respectively, corresponding to an initial CE of 51%. Apparently, the decrease in temperature reduced both the capacity and initial CE of the nanowire anode at a low rate. Nevertheless, the capacity and initial CE of the dual-phase nanowire anode at 273 K and 0.25 C remain better than those of some TiO₂-based SIB anodes at room temperature reported in the literature (Fig. 3d and Table S1). In subsequent cycles, the performance of the electrode

tended to be stable, and the CE reached almost 100% at both temperatures.

Achieving a high rate performance is always a challenge for rechargeable SIBs owing to the difficulty insertion and extraction of Na⁺ into the host structure, and the rate performance of SIBs at low temperatures has not yet been assessed. As mentioned above, introducing heterogeneous interfaces may improve the electrochemical performance of electrode materials. Here we compared the rate performance of nanowires with different phases. As shown in Fig. S7, the dual-phase nanowires exhibited obviously better rate performance than nanowires consisting of only one phase. We then compared the rate performance of the dual-phase nanowire anode at 303 K and 273 K, as shown in Fig. 3a–c. Fig. 3a displays the charge–discharge voltage profiles of the anode at different rates at 303 K. Increasing the rate from 0.25 C to 20 C decreased the reversible capacity from 290.1 to 148.1 mAh g⁻¹. The capacity loss as the rate increased was significant, but the capacity at 20 C remained much higher than the capacities at the same rate reported in the literature (Fig. 3d). Similar rate-performance was obtained for a cell with a larger mass loading at 303 K (Fig. S8). Fig. 3b shows the charge–discharge voltage profiles of the anode at different rates at 273 K. It is interesting that increasing the rate from 0.25 C to 20 C resulted in little capacity loss, as evident in Fig. 3c. This finding implies that the capacity of the dual-phase nanowire anode was almost rate independent at 273 K. Meanwhile, the capacity at 20 C reached 141.5 mAh g⁻¹ at 273 K, which was comparable to that obtained at 303 K and higher than the capacities at room temperature reported in the literature. Fig. 3d compares the rate capabilities of TiO₂-based anodes for SIBs,^{26, 36–43} showing that the performance of dual-phase nanowire anode is among the best. Even at low temperature, the high rate performance of the present dual-phase nanowire anode was much better than the performances reported at room temperature in the literature. We further tested the rate-performance and cycle performance of the dual-phase nanowires at 248 K (Fig. S9 and Fig. S10), and found that, at such a low temperature, the capacity of the nanowires was also relatively high and nearly independent of the current density. A reversible capacity of 122 mAh g⁻¹ was achieved at 10 C and maintained almost constant for more than 1000 cycles. These results demonstrate that the dual-phase TiO₂ nanowire anode possesses excellent rate performance, especially at low temperature, and that its capacity at low temperature is almost rate independent.

The cycling performance of the dual-phase TiO₂ nanowire anode at 303 K and 273 K was measured at 0.5, 1, 5, and 10 C, as shown in Fig. 3e–f, and S11–S13. When cycling at 1 C and 303 K, the nanowire anode showed a high capacity of ~ 250 mAh g⁻¹ in the initial 100 cycles. However, the capacity gradually decreased to ~ 165 mAh g⁻¹ after 200 cycles (Fig. S11). Although the capacity at 1 C and 273 K was ~ 100 mAh g⁻¹ lower than that

obtained at 303 K in the initial 100 cycles, the capacity at 273 K was extremely stable during the 1 C cycling. Even after 1000 cycles, the capacity at 273 K still remained as high as 140 mAh g⁻¹ with neglectable capacity decay. When cycling at a high rate like 10 C, as shown in Fig. 3f, obvious capacity decay was observed at 303 K. However, the nanowire anode exhibits excellent cycling stability at 273 K with an ultralow capacity decay rate of ~0.023% per cycle. Meanwhile, the capacities at 10 C and 1 C when cycling at 273 K were also similar. These results indicate that the dual-phase TiO₂ nanowire anode possesses excellent cycling performance at 273 K at both high and low rates.

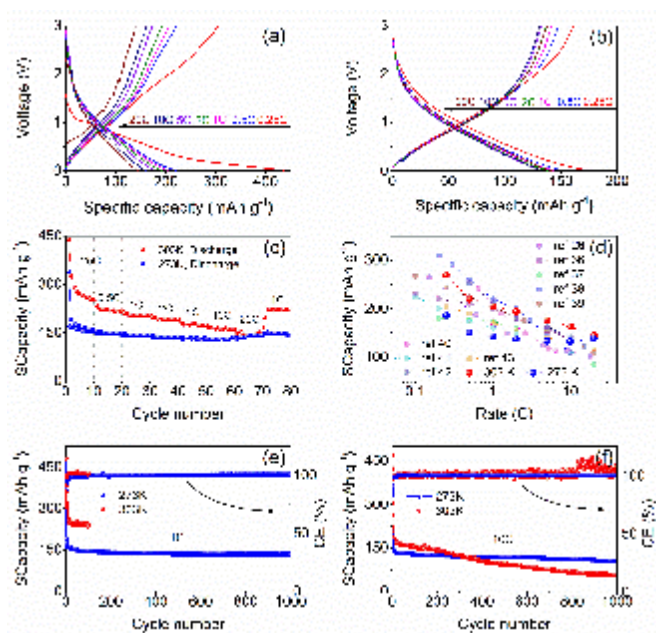


Fig. 3 Electrochemical performance of the dual-phase TiO₂ nanowire anode (SCapacity: Specific capacity). (a, b) The charge–discharge voltage profiles at different rates of 0.25 C–20 C at (a) 303 K and (b) 273 K. (c) Rate performance at different temperatures. (d) Comparison of the rate capability of the dual-phase TiO₂ nanowire anode with other TiO₂-based electrodes reported. (e, f) Cycling performance at rates of (e) 1 C and (f) 10 C at different temperatures.

Structural evolution

To identify the origin of the rate-independent and ultra-stable low-temperature Na-storage performance of the dual-phase TiO₂ nanowire anode, operando Raman spectroscopy, scan rate-dependent CV, temperature-dependent EIS and GITT were conducted to investigate the phase transitions and sodiation kinetics of the anode materials during electrochemical cycling. Fig. 4a and c show the operando Raman spectra of the nanowire anode during 1 C discharge–charge cycle at 303 K and 273 K, respectively. In both cases, the intensities of the Raman peaks gradually decreased with discharging and all peaks nearly disappeared after complete discharge. After complete charge, the

Raman peaks did not reappear at 303 K (Fig. 4b), but those of the TiO₂-B phase reappeared when cycling at 273 K, although the intensities were not as high as those before cycling. Reportedly, the sodiation of anatase TiO₂ results in the formation of an amorphous sodium titanate phase, that functions as the host for Na⁺ storage in the subsequent cycles.⁴⁴ In addition, one study reported the sodiation of TiO₂-B is a single-phase process and that it also leads to the formation of an amorphous host.⁴⁵ In our study, the Raman spectra evolution trend when cycling at 303 K was found to be totally consistent with the above-mentioned sodiation mechanism that the crystalline nanowire transforms into an amorphous structure after cycling. However, when cycling at 273 K, the anatase phase in the nanowire was amorphized, but the TiO₂-B phase remained crystalline. The capacity performance of the nanowire anode was closely related to the structural transition during sodiation–desodiation. The sodiation of TiO₂-B should be an intercalation reaction because of its large d-spacing, followed by the amorphization process. The amorphization process will then lead to a higher capacity than the intercalation reaction. At low temperature, the amorphization of the TiO₂-B phase is inhibited, which explains the reason why lower capacity was observed at 273 K than at 303 K. However, the intercalation mechanism ensures the structure stability of the nanowire during cycling and is beneficial for both the cycling performance and rate performance⁴⁶ because amorphization generally results in large volume expansion and cracks. The operando Raman spectra results indicate that the nanowire structure is more stable during low-temperature cycling than during high-temperature cycling.

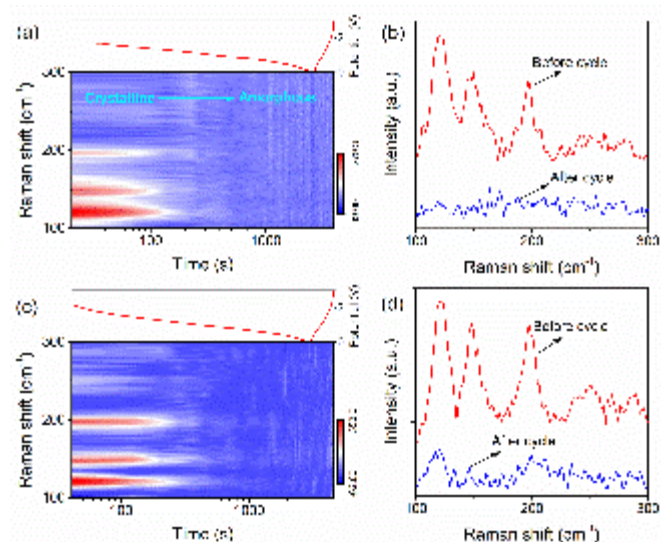


Fig. 4 2D intensity map of the operando Raman spectroscopy of the dual-phase TiO₂ nanowire anode during the first sodiation/desodiation cycle at the rate of 1 C at (a–b) 303 K and (c–d) 273 K. (b) The Raman spectra before and after cycle at 303 K. (d) The Raman spectra before and after cycle at 273 K.

Kinetic analysis

The CV curves of the dual-phase TiO₂ nanowire anode measured at increasing scan rates from 0.1 to 20 mVs⁻¹ at 303 K and 273 K are shown in Fig. 5a, b and S14. All CV curves show similar shapes with broad peaks for Na⁺ insertion/extraction. The neglectable peak shifts with increasing scan rates indicate ultralow polarizations, implying fast Na⁺ diffusion kinetics in the nanowire anode. In addition, the CV results showed that the sodium storage of the dual-phase TiO₂ nanowire anode was controlled by both diffusion and capacitance. The total charge in a CV scan includes the faradaic contributions from pseudo-capacitance and Na⁺ diffusion and a non-faradaic contribution from the double-layer charging.⁴⁷ These capacitive effects can be distinguished from Na⁺ diffusion by analyzing the CV data at various scan rates based on the following relationship:⁴⁸

$$i = au^b \quad (1)$$

where i is the measured current, u is the scan rate, and a and b are coefficients. The value of b can be calculated from the slope of the $\log(i)$ - $\log(u)$ plots. In particular, $b = 0.5$ indicates a total diffusion-controlled process, whereas $b = 1.0$ indicates a capacitive process. Fig. 5c shows that the $\log(i)$ is linearly related to the $\log(u)$. Therefore, the b values at various potentials can be determined using the above relationship, and the results are shown in Fig. 5d. Clearly, the b values at both temperatures are much higher than 0.5, indicating that the sodiation of the dual-phase TiO₂ nanowire anode was a combination of diffusion and capacitance. Meanwhile, the b values are higher at low temperature than at high temperature, indicating that the contribution of capacitive charge was larger at low temperature than at high temperature. Most of the total charge at 273 K originated from the capacitive process. The ultralow polarizations and enhanced capacitive effect at low temperature endowed the dual-phase TiO₂ nanowire anode with excellent rate performance and cycling stability.

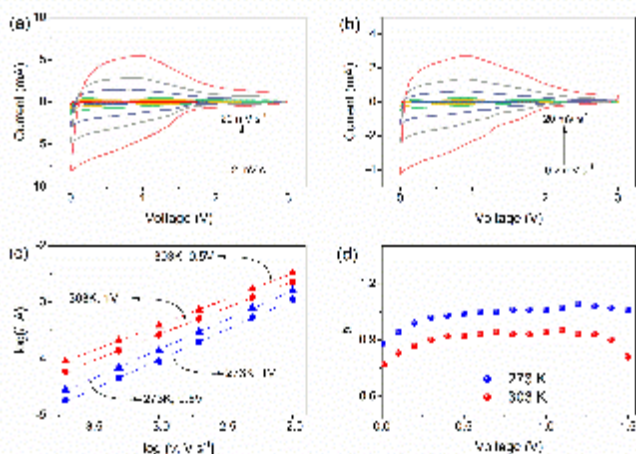


Fig. 5 (a) Cyclic voltammograms (CV) curves of the dual-phase TiO₂ nanowires anode at various scan rates from 0.2 to 20 mV s⁻¹ at 303 K. (b) CV curves at 273 K. (c) The $\log(i)$ vs $\log(u)$ relationship at selected potentials. (d) The b -values at various potentials determined using the relationship between current and scan rate $i = au^b$.

To gain more fundamental insights into the fast Na⁺ diffusion kinetics of the nanowire anode, temperature-dependent EIS and GITT measurements were obtained to investigate the kinetic properties including the charge-transfer resistance and energy barrier and the diffusion coefficient of Na ions in the cell system. Fig. 6a shows the EIS spectra measured at various temperatures. All spectra contain a semicircle, which is related to the charge transfer resistance.⁴⁹ The charge-transfer resistance R_{ct} can be calculated as follows:⁵⁰

$$R_{ct} = RT/(F^2Ak_sx^{0.5}(1-x)^{0.5}) \quad (2)$$

where F is the Faraday constant, T is the absolute temperature, R is the gas constant, k_s is the standard exchange rate constant, A is the total electroactive surface area, and x is the Na concentration. R_{ct} is proportional to T and inversely proportional to A . The charge-transfer resistance of the nanowire anode can be calculated by fitting the EIS spectra using the equivalent circuit shown in Fig. 6b. The charge-transfer resistances at all temperatures were much smaller than those reported for TiO₂-based SIB anodes in the literature (Tables S2 and S3). For example, the resistance was merely 5 Ω at 20 °C. The change in R_{ct} with decreasing temperature was very small. The total electroactive surface area is a crucial factor in determining the capacity especially when cycling at high rates. Thus, when cycling at 273 K at high rates, the anode can exhibit capacities as high as it exhibits when cycling at 303 K. The small change in R_{ct} with decreasing temperature also implies a very low charge-transfer energy barrier, and the charge-transfer energy barrier $E_{a, ct}$ can be calculated by fitting the temperature-dependent resistance, as shown in Fig. 6b. The Arrhenius plot shown in Fig. 6b was used to determine the charge-transfer energy barrier:⁵¹

$$\sigma = T \exp(-E_a/k_B T) \quad (3)$$

Where σ is the ionic conductivity, T is the absolute temperature, A is the pre-exponential factor, E_a is the apparent activation energy for ion transport, and k_B is the Boltzmann constant. The charge-transfer energy barrier calculated using the slope of the line was 79.2 meV, representing a significantly lower charge-transfer energy barrier than that of a previously reported TiO₂/graphene nanocomposite SIB anode.²⁶ This low energy barrier indicates that at any temperature, the transport of Na⁺ was very fast in the cell. The low charge-transfer resistance and energy barrier ensure fast sodiation kinetics and consequent enhancement of the capacitive process, which contributes to the excellent capacity and rate capability of the dual-phase TiO₂ nanowire anode. Fig. 6c and S15 show the GITT voltage profiles and equilibrium potentials of the nanowire anode at 303 K and 273 K. The anode possesses similar polarizations during sodiation-desodiation at different temperatures. The capacity measured by GITT at 273 K was lower than at 303 K, indicating that the capacity performance at low temperature was determined mainly by the active materials. In addition, because GITT measures the theoretically maximum capacity, tailoring the nature of the active materials is an effective way to improve the low-temperature capacity of SIBs. These findings are consistent

with the operando Raman results that the structural change of the active materials is temperature dependent. The apparent Na diffusion coefficients D_{app} at different states of discharge/charge could be calculated using GITT, and the results are shown in Fig. 6d. Clearly, the anode exhibited similar D_{app} during sodiation at different temperatures, indicating that decreasing the temperature did not retard the Na diffusion in the active materials in the current case. Meanwhile, GITT results show that the D_{app} during desodiation was higher at low temperature than at high temperature, which is seemingly contrary to our traditional knowledge that diffusion coefficient increases with increasing temperature. This is probably due to the formation of different structures after discharging at different temperatures. At low temperature, the nanowires remained certain extent of crystallinity after full discharging, while the nanowires were totally amorphized at high temperature. The CV analyses also proved that the Na⁺ intercalation pseudocapacitance dominated significantly at low temperature, indicating faster diffusion kinetics. The higher D_{app} is absolutely beneficial for the rate performance of the nanowire anode at low temperature.

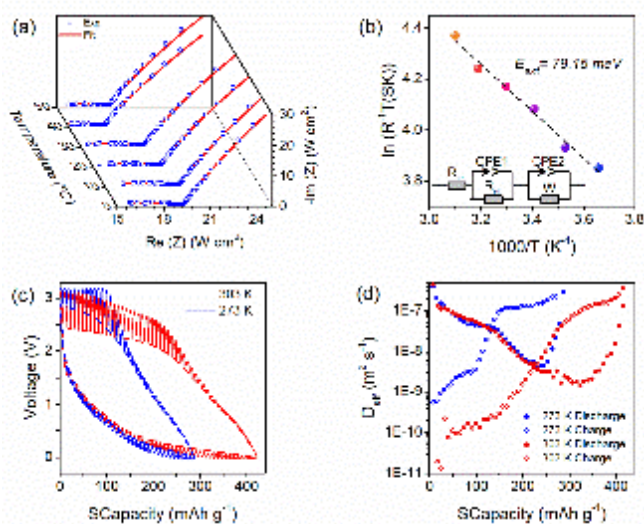


Fig. 6 (a) Temperature-dependent Nyquist plots of the nanowire electrode at various temperatures from 0 to 50 °C. (b) Arrhenius plot of the charge transfer resistance R_{ct} , with the derived charge transfer energy barrier $E_{a,ct}$ and the proposed equivalent circuit for fitting the EIS spectra in Fig. 6a. (c) GITT voltage profiles and equilibrium potentials during sodiation-desodiation. (d) The apparent Na diffusion coefficient D_{app} at various states of discharge/charge determined from the GITT voltage profiles at different temperatures.

Conclusions

In this study, TiO₂-B/anatase dual-phase nanowires were successfully fabricated using a simple hydrothermal and heat treatment method and were applied as SIB anode. The dual-phase TiO₂ nanowire anode showed high rate capability and excellent long-term cycling stability at low temperature. In

particular, increasing the current density from 1 C to 20 C induced only less than 3% reduction of the specific capacity at 273 K. After 1000 cycles at 1 C and 273 K, ~140 mAh g⁻¹ capacity was still achieved, corresponding to an ultralow capacity decay rate of ~0.02% per cycle. Operando Raman spectroscopy showed that the dual-phase nanowires were completely amorphized when cycling at 303 K. However, when cycling at 273 K, only the anatase phase of the nanowires was amorphized and the TiO₂-B phase remained crystalline. The different sodiation mechanism resulted in lower capacity but a more stable structure at low temperature. CV analysis demonstrated that Na⁺ intercalation pseudo-capacitance contributed most of the capacity of the nanowire anode at low temperature. Furthermore, temperature-dependent EIS and GITT verified that the dual-phase TiO₂ nanowires possessed an ultralow charge-transfer resistance and energy barrier and a high apparent Na diffusion coefficient during desodiation, which significantly improved the Na⁺ diffusion kinetics and the capacitive process at low temperature. The synergy between favorable structural transition and fast Na diffusion kinetics provided an excellent Na-storage performance of the dual-phase TiO₂ nanowire at low temperature. The rationale obtained in this work provides a deeper understanding of the effect of low temperature on the Na-storage behavior and an effective strategy to resolve the critical issues of SIB anodes and can be extended to a variety of electrode materials.

Experimental Section

Synthesis of dual-phase TiO₂ nanowires

The fabrication method was similar to that reported by Li.³⁰ First, 2 g of raw TiO₂ nanoparticles (average diameter: 50 nm), purchased from MKnano, M K Impex Corp., were uniformly dispersed in 80 mL of KOH solution (10 M), and the mixture was heated in a 100-mL Teflon-lined autoclave at 200 °C for 24 h. The mixture was then cooled to room temperature. After the hydrothermal treatment, the TiO₂ nanoparticles were transformed to K₂Ti₆O₁₃ nanowires which were then centrifuged and washed three times with deionized (DI) water. The K₂Ti₆O₁₃ nanowires were then ion-exchanged using a 0.5 M HCl solution with homogeneous stirring for 4 h and isolated by centrifugation. The obtained products were washed three times with DI water and dried at 60 °C for 12 h. Finally, the products were heat treated at 350 °C in air for 5 h in a high-temperature muffle furnace to obtain dual-phase TiO₂ nanowires. The fabrication of pure TiO₂-B and anatase phase TiO₂ nanowires was similar to above process, except for the different heat treatment temperatures of 300 °C and 500 °C for TiO₂-B and anatase phase, respectively.

Material characterizations

The morphology and structure of the TiO₂ nanowires were characterized with a STEM (JEOL, JEM-2010F, 200 kV). XRD patterns were recorded on a Rigaku diffractometer equipped

with a Cu K α radiation source operated at 40 kV and 120 mA in the range of 10° to 80°. The Raman spectra were recorded using a MicroRaman system (LabRAM HR spectrometer, Horiba) equipped with an Olympus BX microscope and an argon ion laser (532.05 nm, 50 mW). XPS were recorded using a PHI 5000 VersaProbe II spectrometer with a monochromatic Al K α X-ray source. Nitrogen adsorption–desorption isotherms and the BET surface area were characterized using a Micromeritics ASAP 2020 analyzer.

Electrochemical measurements

For electrochemical measurements, the dual-phase TiO₂ nanowires were mixed with polyvinylidene fluoride (PVDF) and Ketjen black at a weight ratio of 70:10:20 in N-methyl-2-pyrrolidone (NMP). The obtained slurry was then coated on a copper foil and dried in a vacuum oven at 100 °C for 12 h to obtain the working electrode. The 2032 coin-type cells were assembled in an argon-filled glove-box (MBRAUN, MB-OX-SE1), and both moisture and oxygen contents of less than 0.5 ppm were ensured. The Na foil served as the counter electrode, 1.0 M NaCF₃SO₃ in diglyme served as the cell electrolyte, and glass fiber acted as the separator. The galvanostatic charging–discharging measurements were conducted on battery testers (LAND CT-2001A) with voltage windows of 0.01 – 3.0 V for the SIB. The CV tests were performed between 0.01 and 3.0 V. Variable-temperature EIS measurements (0 °C, 10 °C, 20 °C, 30 °C, 40 °C, and 50 °C) were obtained using an electrochemical workstation (PARSTAT 4000) from 105 Hz to 0.1 Hz with a voltage amplitude of 10 mV. GITT measurements were obtained using a current density of 0.5 C (1 C = 335 mA g⁻¹) as the pulse and equal pulse durations of 2.5 min. After each pulse, the cells rested in an open circuit for 2.5 h to reach the equilibrium potential.

Operando Raman spectroscopy

The electrode for the operando Raman measurement was fabricated by mixing the TiO₂ nanowires with polyvinylidene fluoride (PVDF) and Ketjen black at a weight ratio of 70:10:20 in N-methyl-2-pyrrolidone (NMP), coating the mixture on a stainless-steel mesh, and drying the coated mesh in a vacuum oven at 100 °C for 10 h. A delicate airtight electrochemical cell with a quartz window on the top was designed and used for the operando Raman spectroscopy tests. The cell was assembled in an argon-filled glove box (O₂ ≤ 0.5 ppm, H₂O ≤ 0.5 ppm) with Na foil as the counter electrode, and 1.0 M NaCF₃SO₃ in diglyme as the electrolyte. The Raman spectra were recorded using a MicroRaman system (LabRAM HR spectrometer, Horiba) equipped with an Olympus BX microscope and an argon ion laser (532.05 nm). The D2 filter was chosen to avoid electrode degradation. Each spectrum required 20 s measurement-time with two times accumulation. The spectra were collected in the galvanostatic mode because the operando Raman cell was under a constant current density of 1 C (1 C = 335 mA g⁻¹). The galvanostatic discharge–charge cycling of the cell was

controlled using an electrochemical workstation (PARSTAT 4000).

Conflicts of interest

There are no conflicts to declare.

Acknowledgements

D. Lin and K. Li contributed equally to this work. This work was supported by General Research Fund (Grant No. 15210718) from Hong Kong Research Grants Council and Local Innovative and Research Teams Project of Guangdong Pearl River Talents Program (Grant No. 2017BT01N111). D. Lin acknowledged the support by the Hong Kong Polytechnic University.

Notes and references

- J. B. Goodenough, *Acc. Chem. Res.*, 2013, **46**, 1053-1061.
- A. S. Arico, P. Bruce, B. Scrosati, J. M. Tarascon and W. Van Schalkwijk, *Nat. Mater.*, 2005, **4**, 366-377.
- X. H. Lu, M. H. Yu, G. M. Wang, Y. X. Tong and Y. Li, *Energy Environ. Sci.*, 2014, **7**, 2160-2181.
- J. M. Tarascon and M. Armand, *Nature*, 2001, **414**, 359-367.
- X. B. Chen, C. Li, M. Gratzel, R. Kostecki and S. S. Mao, *Chem. Soc. Rev.*, 2012, **41**, 7909-7937.
- H. Yang, H-H. Wu, M. Ge, L. Li, Y. Yuan, Q. Yao, J. Chen, L. Xia, J. Zheng, Z. Chen, J. Duan, K. Kisslinger, X. C. Zeng, W-K. Lee, Q. Zhang and J. Lu, *Adv. Funct. Mater.*, 2019, **29**, 1808825.
- L. Zhao, H-H. Wu, C. Yang, Q. Zhang, G. Zhong, Z. Zheng, H. Chen, J. Wang, K. He, B. Wang, T. Zhu, X. C. Zeng, M. Liu and M-S. Wang, *ACS Nano*, 2018, **12**, 12597-12611.
- J. W. Choi and D. Aurbach, *Nat. Rev. Mater.*, 2016, **1**, 16013.
- B. Qu, C. Ma, G. Ji, C. Xu, J. Xu, Y. S. Meng, T. Wang and J. Y. Lee, *Adv. Mater.*, 2014, **26**, 3854-3859.
- L. David, R. Bhandavat and G. Singh, *ACS Nano*, 2014, **8**, 1759-1770.
- H. Huang, H-H. Wu, C. Chi, B. Huang and T-Y. Zhang, *J. Mater. Chem. A*, 2019, **7**, 8897-8904.
- G. Zhu, K. Wen, W. Lv, X. Zhou, Y. Liang, F. Yang, Z. Chen, M. Zou, J. Li, Y. Zhang and W. He, *J. Power Sources*, 2015, **300**, 29-40.
- B. Yang, H. Zhang, L. Yu, W. Fan and D. Huang, *Electrochim. Acta*, 2016, **221**, 107-114.
- K. Chen, Z. Yu, S. Deng, Q. Wu, J. Zou and X. Zeng, *J. Power Sources*, 2015, **278**, 411-419.
- E. Markevich, G. Salitra and D. Aurbach, *J. Electrochem. Soc.*, 2016, **163**, A2407-A2412.
- A. Varzi, L. Mattarozzi, S. Cattarin, P. Guerriero and S. Passerini, *Adv. Energy Mater.*, 2018, **8**, 1701706.
- N. Zhao, Y. Li, X. Zhao, X. Zhi and G. Liang, *J. Alloys Comp.*, 2016, **683**, 123-132.
- Y. You, H. R. Yao, S. Xin, Y. X. Yin, T. T. Zuo, C. P. Yang, Y. G. Guo, Y. Cui, L. J. Wan and J. B. Goodenough, *Adv. Mater.*, 2016, **28**, 7243-7248.
- J. Z. Guo, P. F. Wang, X. L. Wu, X. H. Zhang, Q. Yan, H. Chen, J. P. Zhang and Y. G. Guo, *Adv. Mater.*, 2017, **29**, 1701968.
- S. Komaba, W. Murata, T. Ishikawa, N. Yabuuchi, T. Ozeki, T. Nakayama, A. Ogata, K. Gotoh and K. Fujiwara, *Adv. Funct. Mater.*, 2011, **21**, 3859-3867.
- Z. Li, J. Ding and D. Mitlin, *Acc. Chem. Res.*, 2015, **48**, 1657-1665.

- 22 D. Y. W. Yu, P. V. Prikhodchenko, C. W. Mason, S. K. Batabyal, J. Gun, S. Sladkevich, A. G. Medvedev and O. Lev, *Nat. Commun.*, 2013, **4**, 2922.
- 23 X. Yu, D. Lin, P. Li and Z. Su, *Sol. Energy Mater. Sol. Cells*, 2017, **172**, 252-269.
- 24 T. Fröschl, U. Hörmann, P. Kubiak, G. Kučerová, M. Pfanzelt, C. K. Weiss, R. J. Behm, N. Hüsing, U. Kaiser, K. Landfester and M. Wohlfahrt-Mehrens, *Chem. Soc. Rev.*, 2012, **41**, 5313-5360.
- 25 G. Q. Zhang, H. B. Wu, T. Song, U. Paik and X. W. Lou, *Angew. Chem. Int. Ed.*, 2014, **53**, 12590-12593.
- 26 C. Chen, Y. Wen, X. Hu, X. Ji, M. Yan, L. Mai, P. Hu, B. Shan and Y. Huang, *Nat. Commun.*, 2015, **6**, 6929.
- 27 Q. Wu, J. Xu, X. Yang, F. Lu, S. He, J. Yang, H. J. Fan and M. Wu, *Adv. Energy Mater.*, 2015, **5**, 1401756.
- 28 Q. Tian, Z. Zhang, L. Yang and S. Hirano, *J. Mater. Chem. A*, 2015, **3**, 14721-14730.
- 29 N. Wang, Z. Bai, Y. Qian and J. Yang, *Adv. Mater.*, 2016, **28**, 4126-4133.
- 30 B. Chen, Y. Meng, F. Xie, F. He, C. He, K. Davey, N. Zhao and S.Z. Qiao, *Adv. Mater.*, 2018, **30**, 1804116.
- 31 Y. Wu, Y. Jiang, J. Shi, L. Gu and Y. Yu, *Small*, 2017, **13**, 1700129.
- 32 L. Wu, D. Buchholz, D. Bresser, L. Gomes Chagas and S. Passerini, *J. Power Sources*, 2014, **251**, 379-385.
- 33 Y. Liu, F. Zhao, J. Li, Y. Li, J. A. Mcleod and L. Liu, *J. Mater. Chem. A*, 2017, **5**, 20005-20013.
- 34 K. Li, B. Li, J. Wu, F. Kang, J. K. Kim and T. Y. Zhang, *ACS Appl. Mater. Interfaces*, 2017, **9**, 35917-35926.
- 35 K. Li, X. Zhou, A. Nie, S. Sun, Y. B. He, W. Ren, B. Li, F. Kang, J. K. Kim and T. Y. Zhang, *Nano Lett.*, 2017, **17**, 1282-1288.
- 36 M. N. Tahir, B. Oschmann, D. Buchholz, X. Dou, I. Lieberwirth, M. Panthofer, W. Tremel, R. Zentel and S. Passerini, *Adv. Energy Mater.*, 2016, **6**, 1501489.
- 37 X. Yang, C. Wang, Y. Yang, Y. Zhang, X. Jia, J. Chen and X. Ji, *J. Mater. Chem. A*, 2015, **3**, 8800-8807.
- 38 Y. Wu, X. Liu, Z. Yang, L. Gu and Y. Yu, *Small*, 2016, **12**, 3522-3529.
- 39 J. Chen, Y. Zhang, G. Zou, Z. Huang, S. Li, H. Liao, J. Wang, H. Hou and X. Ji, *Small*, 2016, **12**, 5554-5563.
- 40 H. Liu, K. Cao, X. Xu, L. Jiao, Y. Wang and H. Yuan, *ACS Appl. Mater. Interfaces*, 2015, **7**, 11239-11245.
- 41 B. Wang, F. Zhao, G. Du, S. Porter, Y. Liu, P. Zhang, Z. Cheng, H. K. Liu and Z. Huang, *ACS Appl. Mater. Interfaces*, 2016, **8**, 16009-16015.
- 42 B. Li, B. Xi, Z. Feng, Y. Lin, J. Liu, J. Feng, Y. Qian and S. Xiong, *Adv. Mater.*, 2018, **30**, 1705788.
- 43 Y. Zhang, C. W. Wang, H. S. Hou, G. Q. Zou and X. B. Ji, *Adv. Energy Mater.*, 2017, **7**, 1600173.
- 44 K. Li, J. Zhang, D. Lin, D. W. Wang, B. Li, W. Lv, S. Sun, Y. B. He, F. Kang, Q. H. Yang, L. Zhou and T. Y. Zhang, *Nat. Commun.*, 2019, **10**, 725.
- 45 J. Lee, J. K. Lee, K. Y. Chung, H-G. Jung, H. Kim and J. Mun, W. Choi, *Electrochim. Acta*, 2016, **200**, 21-28.
- 46 H. Liu, F. C. Strobridge, O. J. Borkiewicz, K. M. Wiaderek, K. W. Chapman, P. J. Chupas and C. P. Grey, *Science*, 2014, **344**, 1252817.
- 47 J. Wang, J. Polleux, J. Lim and B. Dunn, *J. Phys. Chem. C*, 2007, **111**, 14925-14931.
- 48 S. M. Li, L. L. Xie, H. S. Hou, H. X. Liao, Z. D. Huang, X. Q. Qiu and X. B. Ji, *J. Power Sources*, 2016, **336**, 196-202.
- 49 M. D. Levi, G. Salitra, B. Markovsky, H. Teller and D. Aurbach, *J. Electrochem. Soc.*, 1999, **146**, 1279-1289.
- 50 M. Itagaki, N. Kobari, S. Yotsuda, K. Watanabe, S. Kinoshita and M. Ue, *J. Power Sources*, 2005, **148**, 78-84.
- 51 M. R. Busche, T. Drossel, T. Leichtweiss, D. A. Weber, M. Falk, M. Schneider, M. L. Reich, H. Sommer, P. Adelhelm and J. Janek, *Nat. Chem.*, 2016, **8**, 426-434.